CHEMISTRY OF MATERIALS

pubs.acs.org/cm

Article

Investigation of Structural and Electronic Changes Induced by Postsynthesis Thermal Treatment of $LiNiO_2$

Hang Li, Weibo Hua, Björn Schwarz, Martin Etter, Stefan Mangold, Georgian Melinte, Nicola Pietro Maria Casati, Helmut Ehrenberg, and Sylvio Indris*

Cite This: *Chem. Mater.* 2022, 34, 8163–8177

Read Online

ACCESS | Metrics & More | Article Recommendations | Supporting Information

ABSTRACT: Postsynthesis thermal treatments at various temperatures in air have been applied to $LiNiO_2$, and the induced structural and electronic changes have been uncovered. Except for the familiar decomposition process at higher temperatures, a series of transformations also take place under mild conditions. To identify such subtle changes, *ex situ* and *in situ* synchrotron radiation diffraction, *ex situ* ^{7}Li nuclear magnetic resonance spectroscopy, and *ex situ* measurements of magnetic properties have been performed. We show that the reaction between $LiNiO_2$ and CO_2 starts already at a temperature of 200 °C, forming $Li_{1-z}Ni_{1+z}O_2$ layers. If the thickness of this layer is well adjusted, the electrochemical performance of $LiNO_2$ can be improved. A cation off-stoichiometry of $[Li_{0.90}Ni_{0.10}]NiO_2$ is identified at 600 °C even before the decomposition occurs. We also investigate the interplay of the reaction between $LiNiO_2$ and CO_2 with the decomposition at 700 °C. The changes in the Ni oxidation state and local Li environments are also monitored during the whole process.

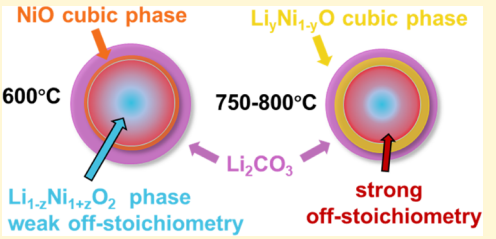

INTRODUCTION

The global electromobile market has expanded a lot during the past decades. This has further stimulated the development of batteries with higher energy density and lower costs.[1,2] The strategies to achieve this goal are to develop new cathodes with higher capacity and stability using cheaper substitutional elements. Nowadays, $LiNi_xCo_yMn_{1-x-y}O_2$ (NCM) and $LiNi_xCo_yAl_{1-x-y}O_2$ (NCA) materials with increased Ni contents have been widely used as cathode materials.[3,4] When the Ni content is increased more and more, finally $LiNiO_2$ (LNO) appears as an end member of the phase system.

Regarding the structure of ideal LNO, it has a cubic close-packed (ccp) array of oxygen atoms. The Li and Ni cations are located in alternating layers in the octahedral vacancies of the oxygen array. Each oxygen has three neighbors of Li and three of Ni, and each cation has six oxygen neighbors.[5] LNO crystallizes as a rhombohedral α-$NaFeO_2$ structure (space group of $R\bar{3}m$). As a widely investigated cathode material in Li-ion batteries, LNO is cheap and offers high energy density but with poor cycling stability.[6] During the synthesis, it is challenging to obtain LNO with a perfect layered structure. "Cation off-stoichiometric" LNO always contains excess Ni^{2+} in the lithium layers due to a Li loss and incomplete oxidation from Ni^{2+} to Ni^{3+}, enabled by a similar radius of Li^+ and Ni^{2+}.[7,8] Other defects possibly also exist, such as Li/Ni antisite defects (site exchange of small amounts of Li and Ni), antiphase domains, and twinning. Layered LNO can be considered to have evolved from the rhombohedral distorted cubic $Li_yNi_{1-y}O$ phase when Li starts to be preferentially incorporated into one layer rather than mixing into the Ni sublattice. Different domains need to merge, and the incoherent interfaces result in the abovementioned defects.[9] Moreover, LNO may even start to decompose during the high-temperature synthesis. Above 700 °C, O and Li losses and Ni reduction occur and the layered phase slowly returns back to a cubic phase.[10] The "reverse process" of the synthetic reaction, i.e., Li and O release instead of uptake, does not likely occur homogeneously throughout the bulk. The surface of LNO in general exhibits a different structure compared with the bulk because during the cooling process after synthesis a gas/solid surface reconstruction reaction has already occurred.[11] Li keeps migrating from bulk to the surface and reacts with CO_2 to form Li_2CO_3. Partial Ni reduction and O loss also occur in this surface structure with a reduced Li content. Even during storage in air, the surface reconstruction occurs when O_2, H_2O, and CO_2 react with LNO to form LiOH, Li_2CO_3, and $LiHCO_3$.[12,13] All of these defects and side reactions could lead to a deterioration of the electrochemical performance.

Concerning thermal stability, delithiated LNO cathodes start to decompose even at lower temperatures. The layered structure undergoes successive phase transitions to a pseudo-spinel, then to a disordered layered structure, and finally to a cubic phase.[14,15] Oxygen release always occurs during later

Received: April 1, 2022
Revised: July 14, 2022
Published: September 6, 2022

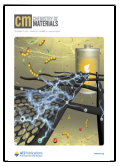

periods of transitions, giving rise to potential safety hazards. Regarding fully lithiated bulk LNO, it starts to decompose above 700 °C, but other reactions may also occur at lower temperatures. These reactions proceed at a low rate and to a small extent, so it is challenging to characterize these reactions, and their effect on the electrochemical performance is often overlooked. To investigate this correlation, a heat treatment in air after synthesis (in pure oxygen) was performed with a 12 h duration to increase the extent of reactions. A series of heat treatment temperatures (from 200 to 1000 °C) are used to investigate how the rate of these subtle reactions changes with temperature. The relationship between these reactions and LNO decomposition is also uncovered. Characterization methods include *in situ* and *ex situ* X-ray diffraction (XRD), *exsitu* ^{7}Li nuclear magnetic resonance (NMR) spectroscopy, *ex situ* X-ray absorption spectroscopy (XAS), transmission electron microscopy (TEM), *ex situ* measurements of magnetic properties, and thermogravimetric analysis (TGA). By combining all of these methods, we aim to provide the full image of reactions in LNO at different temperatures. The possibility of improving the electrochemical performance of LNO solely by postsynthesis thermal treatment is also demonstrated.

EXPERIMENTAL SECTION

Materials and Electrochemistry. *Synthesis of $LiNiO_2$.* NiOH was synthesized through the traditional coprecipitation process. Three solutions were prepared at first: aqueous solution (A) 0.3 L of 2 M $NiSO_4$; (B) 0.3 L of 2 M NH_3 with 2 M NaOH; and (C) 0.2 L of 2 M NaOH. At first, 200 mL of deionized water was added to the 1.2 L reactor with 2 mL of NH_3 in H_2O. Then, the pH value was automatically controlled to 10.7 by adding solution C. Once the pH value was steady, we started adding solutions A and B. The pumping speed was calculated in such a way that the reaction could be finished in 18 h. The precipitate was washed thoroughly with deionized water and dried in an oven at 80 °C overnight.

$LiNiO_2$ (LNO) was then synthesized by calcining the mixture of the precipitates NiOH and LiOH. The two components were ground using a mortar and pestle for 30 min and transferred to the oven. In a pure oxygen atmosphere, the temperature was first increased to 500 °C, maintained for 6 h, and then further increased to 700 °C, where it was kept for another 12 h. The sample was cooled freely in the oven, which normally takes 8−10 h.

Postsynthesis Thermal Treatment of $LiNiO_2$. LNO samples were reheated in air from room temperature to different temperatures (heating rate of 5 °C min^{-1}, 200−1000 °C for 12 h). In the following, these samples are denoted as LNO-"heat treatment temperature" (for example, LNO-200).

Electrochemical Characterization. The slurry for the electrode coating consists of 92 wt % LNO, 4 wt % C65 carbon black, and 4 wt % poly(vinylidene fluoride) (PVDF) binder. Doctor blade coating was used to cast the slurry onto Al foil with a wet thickness of 150 μm. The *N*-methylpyrrolidone (NMP) solvent was removed using the method introduced by Dahn (drying at 120 °C for 3 h in air).[16] Electrodes were cut into disks with 1.2 cm diameter and pressed at a pressure of 100 MPa. The active material loading for each electrode was typically 12 mg cm^{-2}. Before testing, the electrodes were dried in vacuum at 120 °C overnight. The electrochemical performance was evaluated using coin-type half-cells (CR2025). For battery assembly, lithium metal was used as the anode and 50 μL of 1.2 M $LiPF_6$ in ethylene carbonate−ethyl methyl carbonate (EC:EMC = 3:7 by vol %) with 2 wt % vinylene carbonate (VC) was used as the electrolyte. For galvanostatic cycling, an electrochemical window between 2.5 and 4.5 V was chosen. The cells were cycled at a rate of 0.1C (1C = 180 mA g^{-1}). All cells were tested using a VMP3 multichannel potentiostat (Bio-Logic, France). At least two cells were used for each sample to check the reproducibility.

To check if the process of drying (120 °C for 3 h in air for removing NMP) already changes the structure of LNO, X-ray radiation diffraction (XRD, Cu Kα radiation, λ = 1.54 Å) was conducted on samples of LNO-200, LNO-700, and also the corresponding slurries after removing NMP. The powder XRD patterns of these four samples are shown in Figure S1. There is no difference in the intensity of the reflections, confirming that the drying process itself does not act as thermal treatment. The characterization methods performed on the heat-treated LNO thus reflect the crystal structure of cathodes in the electrodes.

Synchrotron Radiation Diffraction and X-ray Absorption Spectroscopy. The crystallographic structure of heat-treated LNO was determined by high-resolution synchrotron radiation diffraction (SRD) with a photon energy of 60 keV (λ = 0.21 Å) at beamline P02.1, storage ring PETRA III at Deutsches Elektronensynchrotron (DESY) in Hamburg, Germany. *In situ* high-temperature SRD (HTSRD) was carried out at the MS beamline of Paul Scherrer Institute (PSI), Villigen, Switzerland.[17] LNO powders were heated in air with a heating rate of 20 °C min^{-1} from room temperature to 900 °C. XRD patterns were collected with steps of 50 °C except for the high-temperature region (750−900 °C), where the interval was set to 25 °C. A MYTHEN II detector was used for obtaining the diffraction images at a synchrotron radiation energy of 24.3 keV (λ = 0.51 Å). The lattice structure parameters and phase fractions were refined using the Rietveld method with the program Fullprof.[18] X-ray absorption spectroscopy (XAS) was performed at the XAS beamline of the KIT Light Source (Karlsruhe). XAS data were recorded at the Ni K-edge (8333 eV) in a transmission mode. Background subtraction and normalization were done with ATHENA software,[19] which is part of the Demeter package. The energy calibration was checked by a Ni metal foil, which was placed between the second and third ionization chambers.

Solid-State Nuclear Magnetic Resonance Spectroscopy. ^{7}Li magic-angle spinning (MAS) NMR experiments were conducted on a Bruker Avance 200 MHz spectrometer at a magnetic field of 4.7 T. Spectra were acquired at a Larmor frequency of 77.8 MHz with 1.3 mm rotors and spinning at 60 kHz. A rotor-synchronized Hahn-echo pulse sequence (90°-τ−180°-τ-acquisition) was used with a 90° pulse length of 0.9 μs and a recycle delay of 1 s. The ^{7}Li NMR shifts were referenced using an aqueous 1 M LiCl solution (0 ppm). All spectra were normalized with respect to sample mass and number of scans.

Thermogravimetric Analysis. The TGA measurement was performed to acquire the mass loss of LNO during heat treatment. It was carried out on an STA 449 F3 Jupiter instrument (NETZSCH) with a heating rate of 5 °C min^{-1} up to 1000 °C in an air atmosphere. The experiment was repeated once to check reproducibility.

Magnetization Measurements. Magnetization as a function of temperature and magnetic field was measured with a physical property measurement system (PPMS DynaCool) from QuantumDesign equipped with a vibrating sample magnetometer (VSM). Zero-field-cooled (ZFC) and field-cooled (FC) magnetization *vs* temperature were measured from 2 to 380 K (for the "pristine" sample only up to 300 K) at a field of 500 Oe. From 2 to 50 K, the heating rate was set to 1 K min^{-1} and from 50 to 380 K it was set to 2 K min^{-1}. Magnetization *vs* field hysteresis measurements with maximal fields of 7×10^4 Oe have been performed at 2 and 300 K in a field-cooled mode starting the field scan with the maximum positive field as specified above. Additionally, magnetization *vs* temperature was measured from 270 to 390 K at a field of 5000 Oe with a rate of 2 K min^{-1}. The data sets from these temperature scans at a higher field were used for Curie−Weiss fits. Additionally, magnetization *vs* field hysteresis measurements were performed at 300 and 390 K with a maximum field of 5000 Oe for in-depth magnetic characterization at higher temperatures. For data evaluation, the sample masses for pristine LNO, LNO-200, and LNO-300 have not been corrected. For LNO-400 to LNO-750 that contain a certain amount of Li_2CO_3, only the masses of the LNO phase have been considered since Li_2CO_3 has a negligible contribution to the magnetic signal. For LNO-800 and LNO-1000 that consist of LNO and a cubic (Li, Ni)O phase, the masses and molar masses have accordingly been corrected assuming

https://doi.org/10.1021/acs.chemmater.2c00995
Chem. Mater. 2022, 34, 8163−8177

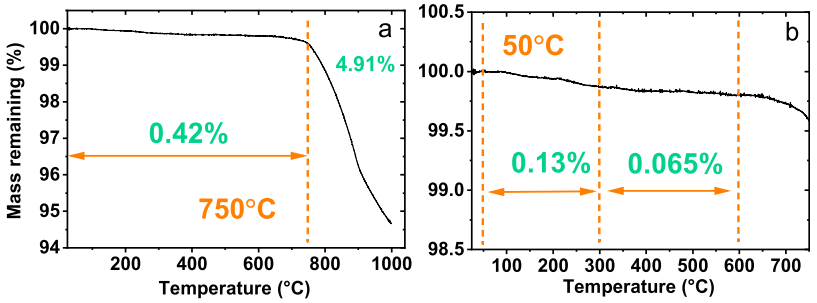

Figure 1. (a) Full-temperature region and (b) enlarged region of TGA measurement on the as-prepared LNO in air from room temperature to 1000 °C (750 °C for panel (b)). The green numbers correspond to the mass loss of denoted regions.

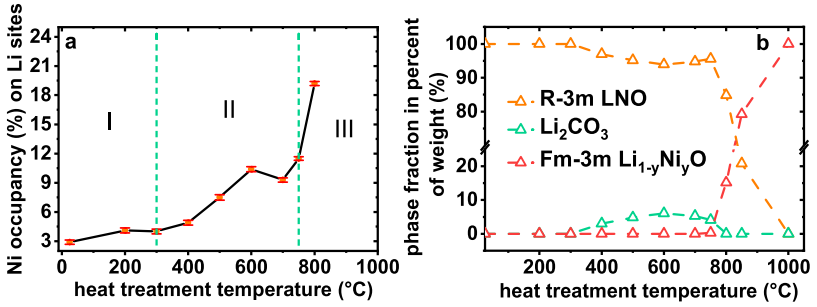

Figure 2. (a) Changes of Ni occupancy on Li sites (%) from the Rietveld refinement results. 25 °C represents the pristine state. Three regions are labeled I, II, and III. (b) The change of phase composition with increasing heat treatment temperatures.

two different types of (Li, Ni)O phase: (a) a Li containing $Li_{0.5}Ni_{0.5}O$ phase that corresponds to $LiNiO_2$ (LNO) and (b) a Li-free NiO phase.

Transmission Electron Microscopy (TEM). To perform TEM measurements, the sample was prepared inside an argon-filled glovebox and then transferred to the microscope using a vacuum transfer holder. To prevent samples from extensive air exposure, the dry powder of the samples was directly dispersed on the TEM holey carbon membrane without the use of solvents. The measurements were performed using a double aberration-corrected and monochromated Themis Z microscope equipped with a Gatan GIF Continuum 970 spectrometer and a K3 IS camera. High-resolution scanning transmission electron microscopy high-angle annular dark-field (STEM-HAADF) images were recorded using a collection angle range of 63−200 mrad. Electron energy loss spectroscopy (EELS) spectrum imaging data cubes were acquired with a probe convergence angle of 30 mrad and a probe current of 0.5 nA. The pixel size was around 1 nm, and a dwell time of 0.1 s per pixel was used for all of the data series. The camera length was 30 mm, and the spectrometer aperture was set to 5 mm resulting in a collection angle of about 40 mrad. All EELS data were acquired in a dual-EELS mode containing both the core loss and the low loss spectra. All core loss spectra were realigned and deconvoluted based on the low loss spectra pairs prior to any data analysis. The original TEM data used for this manuscript can be downloaded from the following address: https://doi.org/10.5445/IR/1000143860.

RESULTS AND DISCUSSION

As-prepared LNO was further heated in air at different temperatures (200, 300, 400, 500, 600, 700, 750, 800, 850, and 1000 °C) for 12 h and slowly cooled to room temperature. As explained in the Experimental Section, these samples are denoted as LNO-"heat treatment temperature" (for example, LNO-200). A TGA measurement was conducted on the as-prepared LNO in air to investigate the mass loss during the heat treatment (Figure 1). This measurement was repeated, and a similar behavior of mass loss was observed (Figure S2). A temperature of 50 °C was chosen as the reference for the original mass of the LNO since the sudden mass drop at the beginning of the experiment might just stem from the removal of moisture. Interestingly, the mass loss within the 50−300 °C temperature region (0.13%) is two times larger than that of the 300−600 °C region (0.065%). The mass loss decreases at higher temperatures since LNO reacts with CO_2 to a larger extent. This will be further discussed in the XRD section. A strong mass loss was found starting from 750 °C. A mass loss of 4.91% was recorded between 750 and 1000 °C, whereas the corresponding value between 50 and 750 °C is only 0.42%. The mass loss at high temperatures is caused by the emission of O_2 occurring during the phase transition from the layered to cubic structure

$$LiNiO_2 \rightarrow \frac{1}{1+z}Li_{1-z}Ni_{1+z}O_2 + \frac{z}{1+z}Li_2O + \left(\frac{z}{2(1+z)}\right)O_2 \quad (1)$$

Herein, $Li_{1-z}Ni_{1+z}O_2$ denotes the decomposition product still possessing a layered structure. After the continuous loss of O and Li, a phase transition occurs and $Li_{1-y}Ni_yO$ will be used to denote the cubic structure.

XRD. To investigate the exact defect type existing in LNO, the Rietveld refinement of the parameters of four different structural models against the SRD data was performed. Detailed information can be found in the Supplementary Material (Figures S2−S5). Additional Ni ions occupying Li sites ($Li_{1-z}Ni_{1+z}O_2$) are considered to be the dominating defect in LNO with a small degree of Li/Ni exchange. The values of Ni occupancy on Li sites and phase fractions for heat-treated samples are displayed in Figure 2a,b, respectively. Three regions can be identified, in agreement with the TGA results described above: (I) pristine to 300 °C, (II) 400−750 °C, and (III) 800−1000 °C. In the first region, a slight change

https://doi.org/10.1021/acs.chemmater.2c00995
Chem. Mater. 2022, 34, 8163−8177

of Ni occupancy on the Li sites is found from 2.9 ± 0.2% for the pristine sample to 4.0 ± 0.2% for LNO-300, without any new phases being formed. In region II, the Ni occupancy on lithium sites exhibits a significant increase from 4.9 ± 0.3% for LNO-400 to 10.4 ± 0.3% for LNO-600.

In this second region, Li_2CO_3 appears. Based on the refinement result, the content of Li_2CO_3 increases from 3.03 ± 0.58% for LNO-400 to a maximum value of 6.08 ± 0.52% for LNO-600 and then decreases to 4.07 ± 0.97% for LNO-750. A representative refinement for LNO-600 containing Li_2CO_3 is displayed in Figure S6. As reported, LNO reacts with CO_2 at room temperature as well as at high temperatures (900 °C).[20] The reaction is described by the following equation

$$LiNiO_2 + 0.5\ CO_2 \rightarrow NiO + 0.5\ Li_2CO_3 + 0.25\ O_2 \quad (2)$$

This reaction is a thermodynamically favored reaction, and Ni^{3+} is reduced to Ni^{2+}. The extent of this reaction is strongly affected by reaction temperature, duration, and atmosphere. Equation 2 is based on high temperatures (above 650 °C) and a pure CO_2 atmosphere.[20] When the reaction takes place at room temperature and in air, $Li_{1-z}Ni_{1+z}O_2$ rather than NiO would form. The equation then changes to

$$LiNiO_2 + \frac{z}{1+z}CO_2 \rightarrow \frac{1}{1+z}Li_{1-z}Ni_{1+z}O_2 + \frac{z}{1+z}Li_2CO_3 + \left(\frac{z}{2(1+z)}\right)O_2 \quad (3)$$

Although eq 3 looks quite similar to the decomposition reaction (eq 2), the two reactions occur under different conditions. The decomposition of LNO will not occur below 700 °C.[10] We will further discuss this point for the sample LNO-700. The rate of eq 3 is very small, and it was reported that Li_2CO_3 with an amount of 6.96% was formed after exposure to pure CO_2 for 6 months at room temperature.[20] A similar amount (6.08 ± 0.52%) was also found in the sample LNO-600 since high temperature (600 °C) and long duration (12 h) have been applied to LNO. Equation 3 is a mass-gaining reaction, but a steady curve is found in the TGA measurement. As discussed above, eq 3 proceeds at a sluggish rate and there is no temperature holding time during this measurement. Therefore, no significant amount of Li_2CO_3 can be formed in the temperature region of 400−600 °C (the content of Li_2CO_3 is far less than that of LNO-400/500/600), and the tiny mass gaining is offset by the Li/O loss. In contrast, there is only Li/O loss from 200 to 400 °C, inducing a clearer mass loss in the TGA measurement.

With the increase of temperature of thermal treatment, the reaction also proceeds to a gradually larger extent. In addition to the increasing amount of Li_2CO_3, the larger progress of the reaction can also be monitored via the strong cation off-stoichiometry of $Li_{1-z}Ni_{1+z}O_2$. The stoichiometry varies from $[Li_{0.95}Ni_{0.05}]NiO_2$ for LNO-400 to $[Li_{0.90}Ni_{0.10}]NiO_2$ for LNO-600. The reaction between LNO and CO_2 also likely occurs even before 400 °C since a cation off-stoichiometry of $[Li_{0.96}Ni_{0.04}]NiO_2$ has already been found for LNO-300. Li_2CO_3 is not observed by XRD after heating to 300 °C because of the small content. Although no cubic $Li_yNi_{1-y}O$ phase is observed in the XRD patterns after heating up to 300 °C, the reaction described by eq 2 can still occur in thin surface regions. This thin cubic layer will be further discussed in the Magnetic Measurement and TEM sections.

Interestingly, the cation off-stoichiometry of LNO-700 ($[Li_{0.91}Ni_{0.09}]NiO_2$) is slightly weaker than that of LNO-600 ($[Li_{0.90}Ni_{0.10}]NiO_2$). This abnormal behavior is contradictory to the higher reactivity according to eq 3 at higher temperatures, but at 700 °C, the bulk decomposition of LNO also occurs (following eq 1). This means that part of the formed Li_2O reacts with CO_2 to form Li_2CO_3 and with O_2 to form Li_2O_2. Li_2O_2 is volatile and could not be observed by XRD.[21] The reaction described by eq 3 was partially suppressed since less Li_2CO_3 (5.29 ± 0.63%) was found when compared to LNO-600 (6.08 ± 0.52%). Equations 1 and 3 describe competitive reactions. Although the decomposition of LNO starts at around 700 °C, it proceeds three times quicker at 800 °C.[8] The suppressed reaction described by eq 3 and the sluggish rate of the reaction described by eq 1 jointly induce the weak cation off-stoichiometry for LNO-700. As a special sample, LNO-700 will be compared to LNO-600 and the detailed difference in the Ni^{2+} location will be analyzed in the NMR and Magnetic Measurement sections.

For LNO-750, as revealed by the Rietveld refinement shown in Figure S7a, the reaction between LNO and CO_2 is further suppressed (indicated by the smaller amount of Li_2CO_3 (4.07 ± 0.97%)) since the decomposition described by eq 1 proceeds at a faster rate at 750 °C. The increased rate of decomposition results in the strongest cation off-stoichiometry of $[Li_{0.88}Ni_{0.12}]NiO_2$ for LNO-750. The distribution of cation off-stoichiometry is likely inhomogeneous through the particle but not observable by the XRD refinement. The strong cation off-stoichiometry may lead to a full cubic phase at the surface, as displayed in Figure S7b. Some tiny reflections belonging to the $Li_yNi_{1-y}O$ cubic phase appear in addition to those from LNO.

In the third temperature region (from 800 to 1000 °C, region (III)), Li_2CO_3 disappears and the decomposition proceeds more rapidly. When the temperature of the thermal treatment surpasses 750 °C, Li_2CO_3 would be completely melted (melting point of Li_2CO_3 is 720 °C[22]) and penetrated into the alumina container used for synthesis. The Rietveld refinement against XRD patterns of LNO-800 and LNO-850 is shown in Figure S8. The cubic phase amounts to 15.2 ± 0.4% for LNO-800 and 88.3 ± 1.0% for LNO-850 of the whole sample material. LNO-800 represents the sample with the highest temperature of heat treatment that still allows us to determine the cation off-stoichiometry ($[Li_{0.81}Ni_{0.19}]NiO_2$) in the layered phase. For LNO-850, the fraction of the layered phase is too small to conduct a reliable refinement on the value of z in $Li_{1-z}Ni_{1+z}O_2$. For LNO-1000, broader reflections compared to those of the LNO phase that can be ascribed to a cubic $Li_yNi_{1-y}O$ phase were observed. This broadening originates from several modifications of the same phase with slightly different lithium contents and lattice parameters. When performing the refinement, the fitting degree could be further improved when more of these similar models were used (Figure S9). It could be reasonably assumed that there is a certain lithium concentration gradient in this material. On the contrary, the reflections from NiO are very sharp and can be well described by the single NiO model (NiO is prepared by calcining NiOH directly at 1000 °C; Figure S10).

To confirm our assumption and investigate the reversibility of structural changes, an additional series of experiments were performed. Samples heated at 400, 600, and 800 °C were

https://doi.org/10.1021/acs.chemmater.2c00995
Chem. Mater. 2022, 34, 8163−8177

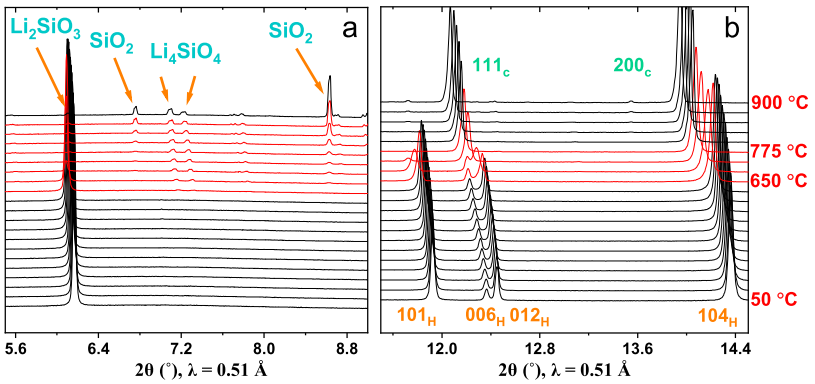

Figure 3. (a) Enlarged regions of *in situ* XRD pattern focusing on the impurities and (b) the change of 101, 006, 012, and 104 reflections during heat treatment. The temperature regions showing impurity formation and phase transition are marked with red colors in panels (a) and (b), respectively.

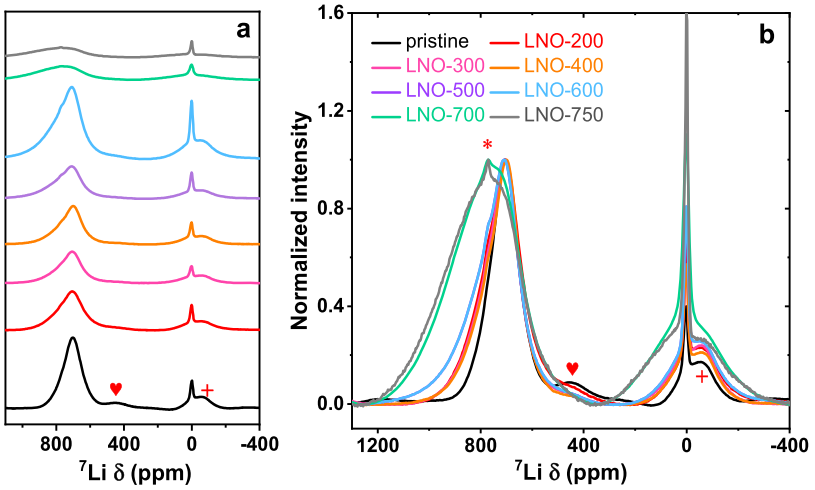

Figure 4. ^{7}Li NMR spectra of pristine LNO and some thermally treated samples. (a) The spectra are stacked with original intensities. The small peak at 425 ppm is labeled with a red heart. (b) The intensity is normalized via the maximum value of the main peak. Asterisks (*) and plus (+) signs indicate the position of spinning sidebands.

reheated in pure oxygen at 700 °C for 12 h. The reheated LNO-400 and LNO-600 samples could return to the pristine state with similar Ni occupancy values on Li sites and performance (Figure S11). The cation off-stoichiometric $Li_{1-z}Ni_{1+z}O_2$ phase could be recovered with surface Li_2CO_3 decomposing and Li ions entering into the layered lattice again. These findings reveal that there is no lithium evaporation at least until 600 °C. For LNO-800, the phase transition to the cubic structure already occurred with severe O and Li losses. As a result, the reheated sample could not recover to its original state. Its capacity is only 140 mAh g^{-1} for the first cycle.

***In Situ* XRD.** *In situ* XRD during heating was performed to trace the structural changes with increasing temperature. Therefore, the quartz capillary was filled with the as-prepared LNO powder and was heated from room temperature to 900 °C (Figure S12). Normally, XRD patterns were collected every 50 °C except for the high-temperature region (750−900 °C), where the interval was set to 25 °C. The change of phase composition is shown in Figure S13 based on the Rietveld refinement against XRD patterns. From room temperature to 600 °C, the original layered phase persists. The lattice parameters keep increasing because of the thermal expansion. When compared with *ex situ* data, z in $Li_{1-z}Ni_{1+z}O_2$ increases at a lower speed (Figure S14) since the temperature was increased at a higher speed (20 °C min^{-1}) and the holding time at each temperature is only 10 min. Under these circumstances, only a small amount of LNO could react with CO_2 and therefore Li_2CO_3 could not be observed, unlike in the *ex situ* measurements performed after heating to 400−600 °C. At 650 °C, new peaks assigned to Li_4SiO_4 are identified (Figure 3a). This compound is formed by the reaction between SiO_2 from the quartz capillary and Li_2O

$$2\,Li_2O + SiO_2 \rightarrow Li_4SiO_4 \quad (4)$$

Meanwhile, the cubic phase $Li_yNi_{1-y}O$ also appears at 650 °C with a weight fraction of 13.5 ± 0.3%. The indication for the $Li_yNi_{1-y}O$ phase comes from what looks like an asymmetry of a series of reflections (such as 104) and the disappearance of diffraction splitting (such as 006 and 012). The cubic phase contributes to the 200 reflection at 2θ angles slightly smaller than those of 104 and 111 reflections and results in the merging of the 006 and 012 reflections (Figure 3b). Note that the formation of Li_4SiO_4 (eq 4) proves that Li_2O is leeched out of LNO during decomposition. Meanwhile, the silicate formation (eq 4) also accelerates the decomposition process (eq 1) by continuously consuming the byproduct Li_2O. This explains why the $Li_yNi_{1-y}O$ phase appears much earlier than in

https://doi.org/10.1021/acs.chemmater.2c00995
Chem. Mater. 2022, 34, 8163−8177

the *ex situ* measurement (at 650 °C for *in situ* and at 750 °C for *ex situ* data). At 700 °C, crystalline SiO_2 appears. The lattice parameter of the cubic phase keeps increasing because the Li content in $Li_yNi_{1-y}O$ is decreasing.[9] Interestingly, at 800 °C, the cubic phase divides into two compositions with different Li amounts (Figure S15). The Li-poor phase should correspond to the outer region of the particles. Another lithium polysilicate (Li_2SiO_3) also forms at this temperature, possibly because there is not enough lithium to form Li_4SiO_4 exclusively. The XRD pattern of LNO-900 with refinement is given in Figure S15 with five phases in total. In summary, the main tendencies of phase transitions are similar to the results obtained from *ex situ* data.

NMR. Solid-state NMR is a very useful tool to investigate the coordination environment of Li. The ^{7}Li NMR shift or hyperfine shift is influenced by the surrounding paramagnetic TM ions mainly by the Fermi-contact interaction.[23] Paramagnetic ions in the first and the second cation coordination shells of Li will induce different NMR shifts. Two different coordinations are distinguished by the bond angle at the bridging oxygen atoms, namely, 90 and 180° bond neighbors. Furthermore, we can expect two paramagnetic species: Ni^{2+} and Ni^{3+} and therefore four different types of bonds for LNO that contribute to the overall NMR shift. Although the exact shift values for each bond contribution are not clear, good estimates can be obtained from results on NCM811: Ni^{2+} (90°): −30 ppm, Ni^{3+} (90°): −15 ppm, Ni^{2+} (180°): 170 ppm, and Ni^{3+} (180°) 110 ppm.[24] Generally speaking, the reduction of Ni^{3+} to Ni^{2+} will induce a left shift in the spectra. To investigate the change in local environments, *ex situ* ^{7}Li NMR spectra of thermally treated samples were measured (Figure 4). To easily make comparisons on peak shifting, some of the spectra were normalized based on the maximum intensity of the main peaks, as shown in Figure 4b. For pristine LNO, the signal is located at around 700 ppm. This large NMR shift can be explained by the local Li environments consisting of 12 Ni^{3+} neighbors, six times linked to Li via 90° oxygen bonds and six times linked to Li via 180° oxygen bonds. For an ideal arrangement with only N^{3+} in the structure and no Li−Ni site exchange, this is the only possible environment around Li. After the replacement of small amounts of Ni^{3+} by Ni^{2+}, aNi^{3+}bNi^{2+} ($a + b = 12$) combinations occur with smaller probability and contribute to the widening of signals. Indeed, the NMR shift for pure Ni^{3+} would be 570 ppm (6×110 ppm $+ 6 \times (-15$ ppm)) if expected values from Ni^{3+} in NCM811 are applied. This difference possibly originates from the influence of Mn on the hyperfine shift in NCM811. There is also a small peak located at 425 ppm labeled with a red heart, which could be ascribed to a Ni-rich rock-salt phase or Li occupancy on Ni sites.[25] This rock-salt phase is electrochemically active and reported to disappear during Li deintercalation.[26] The sharp, narrow peak at 0 ppm originates from diamagnetic impurities such as LiOH and Li_2CO_3.[27] Two different sets of spinning sidebands are labeled with asterisks and plus signs in the spectra. The plus sign denotes the sidebands belonging to the isotropic peak at 700 ppm, and the asterisk labels the sidebands belonging to the peak at 0 ppm associated with diamagnetic lithium salts on the surface. The extended range of ^{7}Li MAS NMR spectra including all sidebands is given in Figure S16.

With increasing heat treatment temperatures, there is no strong change in the shape of the ^{7}Li NMR spectra until 600 °C. However, the NMR peak is already slightly shifted to higher ppm positions for LNO-200. Already for this sample, a slight peak widening can be found after heat treatment. As discussed in the XRD section, the reaction between LNO and CO_2 could occur slowly even at 200 °C following eq 3. When $\frac{Z}{2(1+z)}$ mol O_2 is formed, $\frac{2z}{1+z}$ mol Ni^{3+} is reduced to Ni^{2+}. This reduced Ni^{2+} could induce changes in the NMR shift (−15 ppm for 1 Ni^{3+} replaced by 1 Ni^{2+} (90°) and +60 ppm for 1 Ni^{3+} replaced by Ni^{2+} (180°)). There are no big changes between the spectra of LNO-200, LNO-300, and LNO-400, in accordance with a slow rate of the reaction described by eq 3. The spectra of LNO-500 and LNO-600 look similar, becoming broader with additional intensity at higher ppm values. As discussed in the XRD section, the increase of the Li_2CO_3 content and the z value in $Li_{1-z}Ni_{1+z}O_2$ indicate that the reaction described by eq 3 proceeds to a larger extent. Some Li ions therefore are surrounded by more reduced Ni^{2+} ions. Meanwhile, the intensity of the peak at around 0 ppm also increases in intensity in the temperature region of 400−600 °C (Figure 4b), in accordance with the continuous formation of Li_2CO_3 observed with XRD. For LNO-700, the ^{7}Li NMR peak shows a further strong broadening toward higher ppm values. Based on the XRD refinement, the cation off-stoichiometry of LNO-700 ($[Li_{0.91}Ni_{0.09}]NiO_2$) is slightly weaker than that of LNO-600 ($[Li_{0.90}Ni_{0.10}]NiO_2$). This means that the Ni occupancy on the Li site is not the reason for the broadening and, on average, left shift of the NMR peak observed for LNO-700. The broadening could be ascribed to the formation of more Ni^{2+} during LNO decomposition, as evidenced by XAS (see below). Interestingly, based on eq 1, half of the reduced Ni^{2+} should occupy the Li vacancies and induce a stronger cation off-stoichiometry. That is contradictory to the XRD refinement result. Two possible assumptions could explain this inconsistency: (i) during the decomposition process, although Li vacancies are formed by the formation of Li_2O, not all of them are occupied by the Ni^{2+} but Ni^{2+} is preferentially found in the Ni layer. There is no clear correlation between the cation off-stoichiometry of $Li_{1-z}Ni_{1+z}O_2$ and Ni reduction anymore. (ii) Another assumption is that, still in agreement with eq 1, Ni^{3+} in the Ni layer is preferentially reduced in the Li−O−Ni 180° configuration. Ni^{2+}(180°) has a larger contribution to the NMR shift than Ni^{2+}(90°). The first assumption is more likely and is investigated in detail in the Magnetic Measurements section. For LNO-750, the spectrum is almost identical to that of LNO-700 with a slightly larger peak width. The large difference in cation off-stoichiometry ($[Li_{0.88}Ni_{0.12}]NiO_2$ for LNO-750 and $[Li_{0.91}Ni_{0.09}]NiO_2$ for LNO-700) again is not reflected by the ^{7}Li NMR spectra. As shown in Figure S17, the spectrum of LNO-800 has a slightly larger line width compared to that of LNO-750 and shows a clear left shift (from 799 to 946 ppm). This indicates that the decomposition proceeds at a larger speed and extent. The maximum probability of local Li environments has changed to those with more Ni^{2+} for the first time. For LNO-850, extreme broadening and weak NMR signals are observed since the cubic structure is already present with a weight fraction of 88.3 ± 1.0%. Strongly cation off-stoichiometric $Li_{1-z}Ni_{1+z}O_2$ with a high amount of Ni^{2+} and thus many different Ni^{2+}/Ni^{3+} environments around Li in the remaining layered phase induce enormous broadening. For LNO-1000 that contains exclusively cubic $Li_yNi_{1-y}O$, as evidenced from XRD, the broad component in the spectrum disappears and a very small peak at 27 ppm remains. In accordance with the XRD refinement,

https://doi.org/10.1021/acs.chemmater.2c00995
Chem. Mater. 2022, 34, 8163−8177

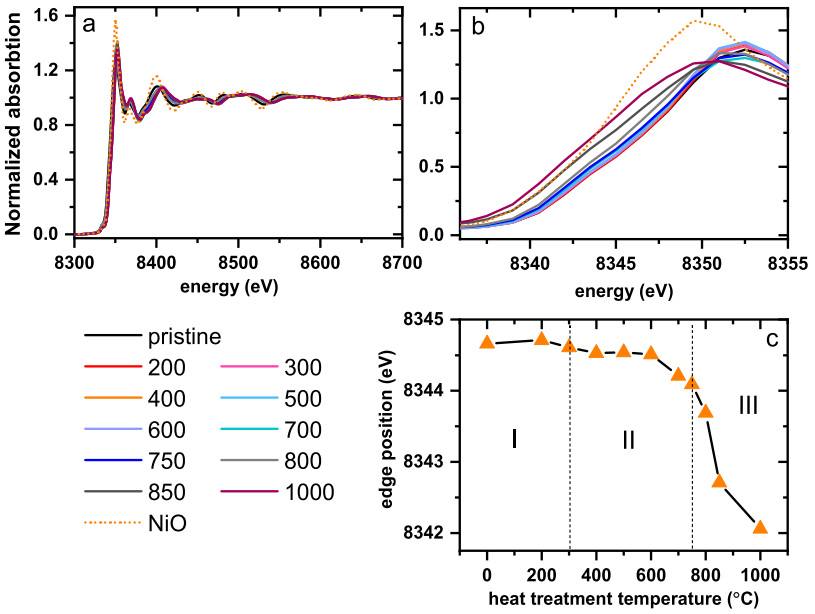

Figure 5. (a) Ni K-edge XAS spectra of the pristine and heat-treated LNO samples and (b) the enlarged view of the edge region. (c) The edge position as defined by the energy where the edge crosses the value 0.55.

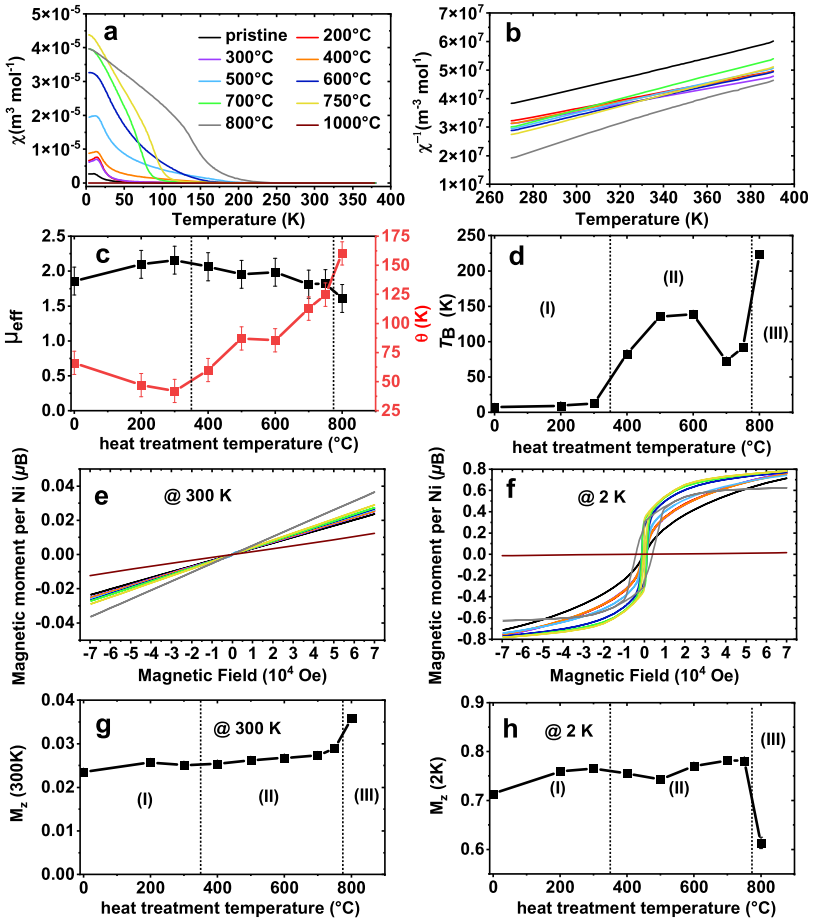

Figure 6. (a) FC curves, (b) the high-temperature inverse susceptibility χ^{-1} measured at 5000 Oe where the part from 340 to 390 K was used for Curie−Weiss fits, (c) the effective paramagnetic moments μ_{eff} in units of Bohr's magneton μ_B and Weiss constant θ, and (d) the change of parameter T_B of the pristine and heat-treated samples. Panels (e) and (f) present the field scans measured at 300 and 2 K up to 7×10^4 Oe, respectively. Panels (g) and (h) display the corresponding z-component magnetizations M_z (300 K) and M_z (2 K), respectively, in units of Bohr's magneton.

https://doi.org/10.1021/acs.chemmater.2c00995
Chem. Mater. 2022, 34, 8163−8177

some Li ions in LNO-1000 are retained in the lattice and also a small amount of Ni^{3+} to keep electric neutrality. The disappearance of the broad contribution might just be related to an even stronger broadening caused by more Ni^{2+}. The very small peak at 27 ppm has a larger width than the peaks close to 0 ppm observed for the lower heating temperatures. This might hint at a diamagnetic phase, such as Li_2O, in close proximity to paramagnetic particles like the cubic $Li_yNi_{1-y}O$. In summary, the change of NMR shifts mainly reflects the Ni reduction process in the layered phase.

XAS. To capture the Ni reduction process, *ex situ* XAS was performed on LNO and heat-treated samples (Figure 5a,b). The Ni K absorption edge shifts toward lower energy with increasing heat treatment temperatures, revealing the successive reduction from Ni^{3+} to Ni^{2+}. However, the rate of reduction is not constant. To clearly show the change in rate, the edge position, defined as the position where the normalized spectrum reaches the value 0.55, is plotted as a function of heating temperature in Figure 5c. From the pristine state to 600 °C, there is only a slight change in the position of the Ni K absorption edge. In this temperature region, LNO reacts with CO_2 and the slight Ni reduction could also be reflected by the increased z value in the $Li_{1-z}Ni_{1+z}O_2$ phase. A more obvious change in edge position occurs between the spectra of LNO-600 and LNO-700. As suggested by the ^{7}Li NMR spectra, more Ni^{2+} is formed during the LNO decomposition at 700 °C and a large fraction is located in the Ni layers. When the heating temperature reaches 800 °C, the rate of Ni reduction increases, corresponding to the phase transformation to the 15.2 ± 0.4% $Li_yNi_{1-y}O$ phase. A strong shift in edge position occurs when comparing the spectra of LNO-800 and LNO-850. Most of the Ni^{3+} has been reduced to Ni^{2+} accompanied by the drastic Li and O losses and phase transition to a large extent (88.3 ± 1.0%). Finally, a pure $Li_yNi_{1-y}O$ phase is formed in LNO-1000 with further O loss. There is a difference in the spectra of LNO-1000 and standard NiO samples since a small amount of Ni^{3+} is still maintained to keep electron neutrality. In summary, a massive reduction of Ni ions is the driving force for the phase transitions.

Magnetic Measurements. As outlined in detail in the reference,[28] Ni^{3+} ions within the Ni layer in LNO are coupled ferromagnetically (FM) due to the ∼90° Ni−O−Ni intralayer coupling paths. In hypothetical stoichiometric LNO without any Ni ions present in the Li layer, the very weak intrinsic interlayer antiferromagnetic (AF) coupling would finally lead to a three-dimensional AF ordering of the Ni layers at low temperature. However, when excess Ni^{2+} is located in the Li layer, it couples antiferromagnetically to the Ni^{3+} ions in both adjacent Ni layers via an ∼180° Ni−O−Ni coupling path with a resultant net FM Ni interlayer coupling that is in frustration to the weak intrinsic AF interlayer coupling. At low concentrations of Ni^{2+} in the Li layer, this leads to a spin glass-like behavior as also observed for the pristine LNO in this work. Since the ferromagnetic intralayer coupling Ni^{2+}−O−Ni^{3+} is stronger compared with the Ni^{3+}−O−Ni^{3+} intralayer coupling, the presence of Ni^{2+} within the Ni layer (due to reduction of Ni^{3+} for instance) in the direct vicinity to Ni^{2+} in the Li layer leads to the formation of localized ferrimagnetic clusters that are in magnetic frustration with their direct surrounding.

Electronic configuration, effective paramagnetic spin-only moment μ_{eff}, and spin-only z-component of the saturation magnetization μ_z for Ni^{2+} and Ni^{3+} in octahedral coordination are listed in Table S1. As can be inferred from the ZFC/FC curves all shown individually in Figure S18 (FC curves are put together in Figure 6a), all samples, except for LNO-1000, exhibit a (predominantly) Langevin paramagnetic region at a higher temperature that is caused by localized magnetic moments formed by the unpaired electrons of the Ni d electrons. It is characterized by a Curie−Weiss behavior with linear dependence of inverse magnetization on temperature. LNO-1000 exclusively consists of the cubic $Li_yNi_{1-y}O$ phase that orders antiferromagnetically at a high Néel temperature T_N = 524 K[29] and therefore does not show paramagnetic behavior within the investigated temperature region. The linear part from 340 to 390 K of the high-temperature susceptibility curves χ^{-1} has been used for a fit with the Curie−Weiss law (see Figures 6b and S19): $\chi^{-1} = \left(\frac{C}{T-\theta}\right)^{-1}$, with Curie constant C, temperature T, and Weiss constant θ. From the Curie constant C, the effective paramagnetic moments μ_{eff} in units of Bohr's magneton μ_B have been determined and are plotted in Figure 6c together with the Weiss constants θ. There is no clear trend observable for the evolution of the paramagnetic effective moment μ_{eff} that evolves around approximately 2 μ_B that is the reported value for $LiNiO_2$ in the literature.[30,31] The Weiss constant θ is positive for all samples, indicating an overall dominating ferromagnetic (FM) coupling. Its value is first only slightly decreasing in region (I) but is then monotonically increasing up to LNO-800, revealing a corresponding increase of the FM-dominated coupling strength. The high-temperature hysteresis measurements (Figure S20) of several samples exhibit a very small contribution from an additional FM phase (deviation from pure linear behavior around the origin) that is equally strong at 300 and 390 K pointing to the existence of small amounts of a reported FM monoclinic NiO phase with T_c = 808 K[32] and a saturation magnetization of about 2.5 Gauss per gram at 300 K that is supposed to have formed at the surface during the heat treatment (see also TEM results); 5.0(1) wt % of this FM NiO phase would cause the observed residual magnetization as determined from a linear fit from 2000 to 1000 Oe of the field scan at 300 K for LNO-400, for instance. This sample reveals the presence of the FM phase quite clearly. The presence of this very small amount of the FM additional phase at the surface with approximately constant magnetization over temperature principally causes very slight deviations from a pure linear evolution of the inverse susceptibility *vs* temperature, and the error bars for the extracted parameters (μ_{eff} and θ) are not simply determined as a statistical error according to the linear fit but include a measure for the uncertainty due to the very slight bending of the χ^{-1} curves. At lower temperatures, a bifurcation of the ZFC and FC branches can be observed with a strong dependence of the temperature of bifurcation on the temperature of heat treatment. As a first parameter of interest, the temperature T_B as the onset of a bifurcation of the ZFC and FC curves, arbitrarily defined here as the temperature where the difference of the magnetic susceptibilities of the ZFC and the FC curves exceeds 2×10^{-7} m^3 mol^{-1}, was determined and is plotted in Figure 6d. In region (I), T_B is comparably small with values slightly varying around 10 K. Region (II) is characterized by a significant increase of T_B with maximal values for LNO-500 and LNO-600 and a decrease again for LNO-700 and LNO-750. Region (III) is characterized by a tremendous increase of T_B for LNO-800 again. Figure 6e,f presents the field scans measured at 300

https://doi.org/10.1021/acs.chemmater.2c00995
Chem. Mater. 2022, 34, 8163−8177

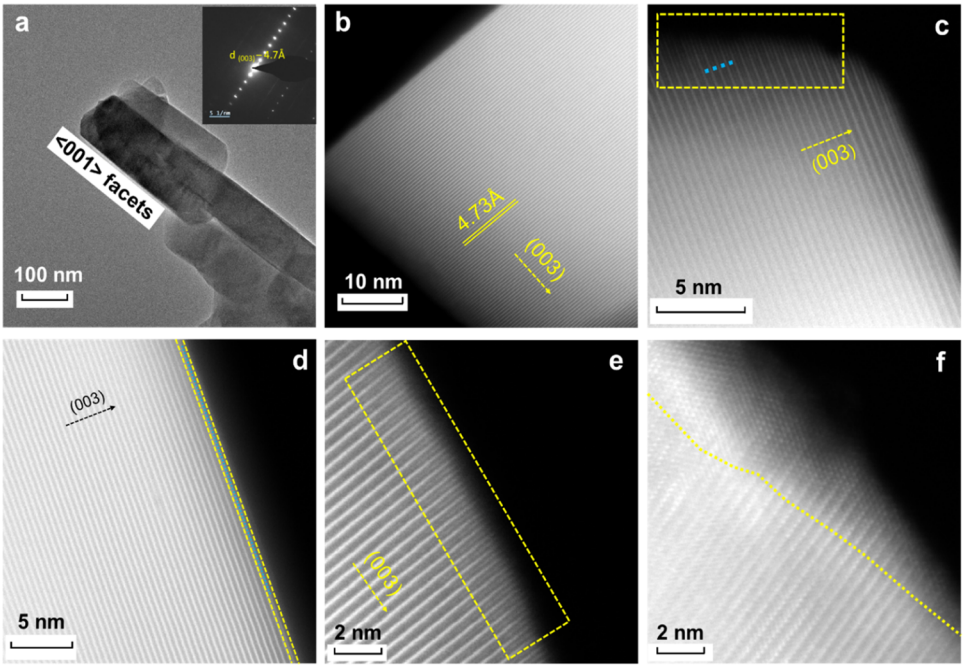

Figure 7. (a) Low-magnification TEM image of LNO particles with the corresponding electron diffraction pattern shown as the inset; (b) high-magnification TEM image of LNO with an interplanar spacing of (003) being labeled; HAADF image of LNO-200 with the strongly cation off-stoichiometric $Li_{1-z}Ni_{1+z}O_2$ region (c) parallel and (d) normal to the (003) direction marked by the yellow boxes; the blue dots denote the Ni^{2+} migrating to Li sites with increased intensity on the Li column. HAADF image of LNO-400 with (e) the strongly cation off-stoichiometric $Li_{1-z}Ni_{1+z}O_2$ region and (f) thin cubic phase on the particle surface.

and 2 K up to 7×10^4 Oe (a series of individual field scans at 2 K to illustrate more clearly the evolution of the coercivity fields is given in Figure S21). The parameters of interest obtained from these field scans are (i) the *z*-component magnetization M_z (300 K) measured at 7×10^4 Oe and 300 K (Figure 6g), (ii) the *z*-component magnetization M_z (2 K) measured at 7×10^4 Oe and 2 K (Figure 6h), and (iii) the coercivity field CF (2 K) extracted from the field scans at 2 K (Figure S22). The higher the temperature of the magnetization measurements, the weaker is the influence of magnetic exchange coupling, anisotropies, and other forms of magnetic interactions, i.e., the values of magnetization are closer to those of the free ion case. Therefore, M_z (300 K) can be considered to return information about the magnetic moment per Ni ion in the first place, whereas M_z (2 K) more strongly includes the effects of interactions of magnetic ions that strongly depend on structural features. M_z (300 K) only slightly increases with the temperature of heat treatment up to 750 °C (see Figure 6g), revealing a slightly increasing magnetic moment per Ni on average. For LNO-800, M_z (300 K) is considerably larger and decreases drastically again for LNO-1000 since here we have a strong antiferromagnetic order present even at 300 K. M_z (2 K) is also varying only slightly for temperatures up to 750 °C, showing a local minimum for LNO-500 (see Figure 6h). All M_z (2 K) values do not exceed 0.8 μ_B per Ni ion and remain well below the expected spin-only saturation *z*-magnetization of 1 μ_B expected for a free Ni^{2+} ion that would be reached at 2 K and 7×10^4 Oe in the free ion case. This means that some sort of antiferromagnetic sublattice coupling and/or anisotropies play a major role here by reducing the observed ordered magnetic moment. M_z (2 K) for LNO-1000 is close to zero due to the antiferromagnetic order that is established almost completely at a low temperature. The evolution of the coercivity fields CF (2K), as shown in Figure S22, is analogous to that of the evolution of T_B. CF (2 K) values up to 300 °C are comparably small and are close to zero for LNO-300. In region (II), the values are increasing first and then decreasing again, very similar to the values of T_B. Again, region (III) (LNO-800) has a characteristic very high value of coercivity. The hysteresis curve of LNO-1000 consisting only of antiferromagnetic NiO does not show any coercivity.

The observed evolution of magnetic properties can be correlated as follows with structural changes as induced by the heat treatment: up to 300 °C (region (I)), there are only minor effects on the magnetic properties. Only a slight increase of M_z (300 K) and μ_{eff} indicates a somewhat increasing magnetic moment due to the reduction of some Ni^{3+} to Ni^{2+}, as also revealed by XAS, that corresponds well with the slow reaction kinetics between LNO and CO_2 as outlined above. In region (II), M_z (300 K), as a representative parameter of the average magnetic moment per Ni ion, still only shows a very slight increase with heat treatment temperature in agreement with the results from XAS measurements. In contrast, those parameters related to the magnetic coupling strength of the Ni ions that are connected to the spatial distribution of the Ni ions within the layered structure and their electronic state change significantly. When a Ni^{3+} is reduced to Ni^{2+} and migrates to the Li layer (as inferred also from the XRD measurements), the effective Ni interlayer FM coupling is enhanced. Additional reduction of neighboring Ni^{3+} to Ni^{2+} within the Ni layer further increases the local FM Ni intralayer coupling and both processes together result in the formation of localized ferrimagnetic clusters that are frustrated with their direct magnetic environment. This is evident for region (II) where we observe a monotonic increase of the dominant FM coupling strength parameterized by the Weiss constant θ with increasing temperature of heat treatment and also the increase of the temperature where a magnetic (frustrated) ordering sets

https://doi.org/10.1021/acs.chemmater.2c00995
Chem. Mater. 2022, 34, 8163−8177

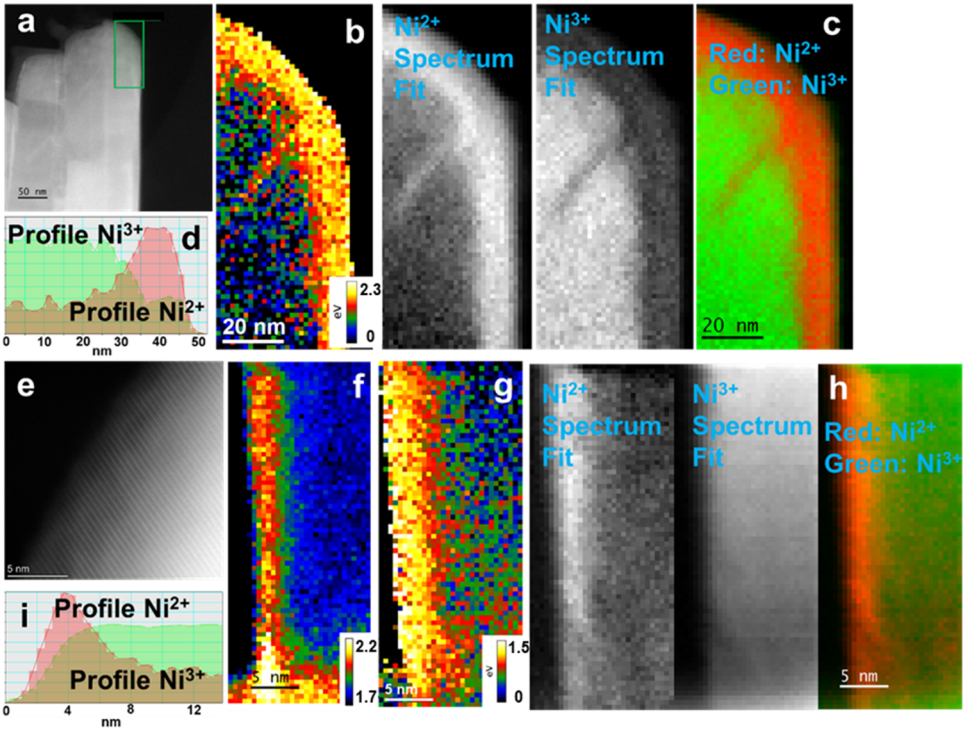

Figure 8. (a) Low-magnification TEM image of LNO-400, (b) the corresponding EEL spectra-based Ni L-edge chemical shift, (c) Ni oxidation state mapping marked with the green rectangle in panel (a), and (d) the profile of the bulk and surface fitting, revealing the concentration of Ni^{2+}/Ni^{3+}. EEL spectra-based analyses on LNO-700: (e) high-magnification TEM image, (f) Ni M-edge/Li K-edge ratio mapping, (g) Ni L-edge chemical shift mapping, and (h) the mapping of Ni^{2+}/Ni^{3+} distribution. Panel (i) shows the relative concentration of Ni^{2+}/Ni^{3+}.

in shifts to higher temperatures, as confirmed by the evolution of T_B. The coercivity field at 2 K CF(2 K) also increases concomitantly with T_B, which might be related to an increasing "pinning" of the localized frustrated ferrimagnetic clusters. However, T_B and CF(2 K) are significantly reduced again for LNO-750 since around 700 °C, the decomposition of LNO within the bulk starts to occur and a large part of Ni^{2+} ions stays in the Ni layer rather than occupy Li vacancies in the Li layer (small value of z in $Li_{1-z}Ni_{1+z}O_2$ in XRD compared with that of 600 °C but a large amount of reduced Ni^{2+} in Ni layers suggested from NMR and XAS). The highest observed value for the coercivity field CF(2 K) for LNO-800 can be explained by a pronounced hindering of magnetic domain wall movement due to the multiphase nature of this sample consisting of LNO and (Li, Ni)O phase. LNO-1000, on the other side, has dramatically changed by losing a lot of oxygen and a transformation from LNO to the $Li_yNi_{1-y}O$ phase that orders antiferromagnetically and exhibits a totally different magnetic behavior compared with the temperature-treated LNO sample series.

TEM. High-resolution STEM was performed to get more insights into local changes in the crystal structure. For pristine LNO, small particles (several hundred nanometers) were used and the layered structure can be clearly identified by electron diffraction (Figure 7a) and high-resolution high-angle annular dark-field (HAADF) imaging (Figure 7b). The d spacing of 4.73 Å corresponds to the (003) atomic plane in the rhombohedral phase. Based on the EELS spectrum imaging data and more exactly on the Ni L3-edge chemical shift mapping, Ni reduction already occurs on the LNO particle surface, proving the existence of the cation off-stoichiometric $Li_{1-z}Ni_{1+z}O_2$ phase (Figure S23). This is shown by the Ni L3-edge 1 eV shift toward lower energies (855 eV for bulk and 854 eV for surface) and also by the diminishing of the O K-edge prepeak in the surface regions (Figure S23c). After the heat treatment at 200 °C, the image contrast on the particle surface has changed both in parallel (Figure 7c) and normal (Figure 7d) to the (003) direction. In the HAADF regime, the contrast is proportional to the atomic number ($\sim Z^{1.7}$).[33] When Ni^{2+} migrates to Li sites, the increase of Z leads to an increased contrast in the regions marked by yellow boxes. The slightly stronger cation off-stoichiometric $Li_{1-z}Ni_{1+z}O_2$ phase is formed through the reaction between LNO and CO_2 (eq 3).

When the heat treatment temperature is increased to 400 °C, an obviously thicker $Li_{1-z}Ni_{1+z}O_2$ phase was observed along the particle surface in Figure 7e. In some regions, the cubic structure could be recognized (such as that in Figure 7f) in HAADF images, which is in accordance with the ferromagnetic NiO phase in the magnetic measurement. This cubic phase is formed from the $Li_{1-z}Ni_{1+z}O_2$ phase with extremely strong cation off-stoichiometry. The off-stoichiometry in the bulk (observed by XRD) and at the surface (observed by TEM) before 700 °C are both induced by the reaction between LNO and CO_2 (eq 3). At the surface, the reaction proceeds to a larger extent because of the direct contact between LNO and CO_2. In the bulk, the reaction also occurs possibly by the migration of Li from the bulk to the Li vacancies at the surface; otherwise, the cation off-stoichiometry would not be observed by XRD. An inhomogeneous distribution of z in $Li_{1-z}Ni_{1+z}O_2$ could therefore exist but is not confirmed neither by XRD nor by TEM images.

To further investigate the structural change in LNO-400, electron energy loss spectroscopy spectrum imaging mapping (EELS−SI) was performed. The corresponding spectra of O K-edge and Ni L-edge at the surface and in the bulk are provided in Figure S24. The Ni L-edge chemical shift map of

https://doi.org/10.1021/acs.chemmater.2c00995
Chem. Mater. 2022, 34, 8163−8177

Table 1. Summary of Relevant Information of Thermally Treated Samples[a]

name	heat treatment 12 h in air (°C)	phase composition	Ni located in the Li layers (%)	weight of Li_2CO_3 (%)	edge position in XPS (eV)	T_B (K) in PPMS
pristine		$R\bar{3}m$	2.9 ± 0.2	0	8344.66	7.35
LNO-200	200	$R\bar{3}m$	4.1 ± 0.2	0	8344.71	9.23
LNO-300	300	$R\bar{3}m$	4.0 ± 0.2	0	8344.61	12.76
LNO-400	400	$R\bar{3}m$	4.9 ± 0.3	3.0%	8344.53	82.9
LNO-500	500	$R\bar{3}m$	7.5 ± 0.3	4.8%	8344.54	135.7
LNO-600	600	$R\bar{3}m$	10.4 ± 0.3	6.1%	8344.51	138.8
LNO-700	700	$R\bar{3}m$	9.3 ± 0.2	5.3%	8344.21	72.6
LNO-750	750	99% $R\bar{3}m$ 1% $Fm\bar{3}m$	11.5 ± 0.2	4.1%	8344.09	91.4
LNO-800	800	85% $R\bar{3}m$ 15% $Fm\bar{3}m$	19.2 ± 0.2	0	8343.69	223
LNO-850	850	21% $R\bar{3}m$ 79% $Fm\bar{3}m$		0	8342.71	
LNO-1000	1000	$Fm\bar{3}m$		0	8342.06	

[a]The shift of edge position in X-ray photoelectron spectroscopy (XPS) corresponds to the continuous reduction of Ni. The temperature T_B in PPMS indicates the number of Ni^{2+} ions located in the Li layers, corresponding to the value in the fourth column, i.e., the value of Ni located in the Li layers obtained by the Rietveld refinement.

the selected green region (Figure 8a) is shown in Figure 8b. The yellow region at the surface shows that a large amount of Ni ions has an oxidation state lower than 3+. This area is larger than that in the HAADF image since only higher occupancy of Ni on lithium sites could induce an obvious contrast change in STEM. The yellow-coded region (thickness of 10−12 nm) covers a wider range of cation off-stoichiometry in $Li_{1-z}Ni_{1+z}O_2$ or NiO phase. As discussed in the XRD and NMR sections, the gradual Ni reduction corresponds to the increase of z in $Li_{1-z}Ni_{1+z}O_2$ before thermal treatment at 700 °C. The inhomogeneous distribution of Li could therefore also be reflected in Figure 8b. Figure 8c shows the Ni oxidation state mapping based on the multiple linear least-squares (MLLS) fitting of the 520−950 eV spectral region, those including both O K-edge and Ni white lines. The thickness of the reduced Ni layer increases to about 15 nm since a wider range of cation off-stoichiometry in $Li_{1-z}Ni_{1+z}O_2$ phase is revealed by this method. The pure red color at the surface corresponds to the ferromagnetic NiO phase found in the magnetic measurements. The profile of the bulk and surface fitting is shown in Figure 8d, revealing the proportion of Ni^{2+} and Ni^{3+} in the two regions approximately. Small amounts of Ni^{2+} ions still exist in the bulk, in accordance with the cation off-stoichiometry of LNO observed by XRD.

Figure 8e shows the HAADF image of the LNO-700. To clearly investigate the structural change in this sample, EELS−SI was also performed with Li K-edge; Ni M/L-edge spectra are shown in Figure S25. Ni M-edge/Li K-edge map was first plotted to evaluate the Li loss situation at the particle surface in Figure 8f. There is a Li-poor region at the surface with a thickness of 3−4 nm and a thin transitional area (dark green area) with a medium concentration of Li. As discussed in the XRD section, the decomposition of LNO occurs at 700 °C but at a slow speed and inhomogeneously. The Li-poor region corresponds to the area with the strongest cation off-stoichiometry of LNO. A large amount of Li ions has been lost, and the vacancies are occupied by Ni ions. A small extent of Li/Ni mixing (Li also migrates to Ni layers) could occur in this area, but no evidence was found to prove this. The neighboring Li transitional area represents the weaker cation off-stoichiometry in $Li_{1-z}Ni_{1+z}O_2$ and also the intermediate states of different decomposition extents between the bulk and surface. The information about the Ni oxidation state could be acquired from Figure 8g, the Ni L-edge chemical shift map of the same area. When compared with the thickness of regions with reduced Ni for LNO-400, it is even getting thinner at 700 °C. As discussed in the XRD section, eqs 1 and 3 described competitive reactions. The reaction of eq 3 is therefore suppressed and that of eq 1 proceeds at a sluggish rate. The actual extent of Ni reduction at the surface of LNO-700 is, therefore, smaller than that of LNO-400. Figure 8h shows the Ni oxidation state mapping based on the MLLS fitting of the O K-edge. The corresponding intensity profile is provided in Figure 8i. Results similar to those in Figure 8f could be obtained. There is a maximum concentration of Ni^{2+} at the surface, corresponding to the Li-poor and Li transitional regions in Figure 8e. Although not obvious in Figure 8g, a certain concentration of Ni^{2+} still exists behind the maximum and decreases slowly into the bulk. This portion of Ni^{2+} corresponds to those located at Li sites and Ni sites, induced by the bulk decomposition of LNO. In summary, TEM analysis mainly reveals the reactions at the surface but that does not mean reactions according to eqs 1 and 3 occur exclusively in surface regions. The cation off-stoichiometry in $Li_{1-z}Ni_{1+z}O_2$ exists both in the bulk and at the surface but to different degrees. Extremely large z in $Li_{1-z}Ni_{1+z}O_2$ or phase transitions to the cubic phase occurs earlier at the surface but in a limited and ultrasmall area.

Table 1 lists the essential information of thermally treated samples provided here as a summary of all characterization methods.

Electrochemical Performance. To investigate the influence of the heat treatment on the electrochemical performance, selected samples were used to prepare cathodes that were tested in coin-type half-cells. Table 2 summarizes most of the electrochemical data. Figure 9a shows the cycling performance of pristine LNO, LNO-200, LNO-300, and LNO-400 cycled galvanostatically between 2.5 and 4.5 V at 0.1C (18 mA g^{-1}) at 25 °C. The weak structural changes in LNO-200 and LNO-300, e.g., the formation of $Li_{1-z}Ni_{1+z}O_2$ phase and ultrathin cubic layers, result in tiny differences in the electrochemical performance compared to those in the pristine

https://doi.org/10.1021/acs.chemmater.2c00995
Chem. Mater. 2022, 34, 8163−8177

Table 2. Summary of the Electrochemical Performance of All Heat-Treated Samples

name	initial discharge capacity (mAh g^{-1}) 2.5−4.5 V 0.1C	capacity retention after 50 cycles (%)
pristine	229	64.7 ± 2.4
LNO-200	231	64.7 ± 2.4
LNO-300	224	63.0 ± 2.1
LNO-350	212	73.6 ± 2.2
LNO-360	212	80.3 ± 2.6
LNO-370	195	82.9 ± 3.5
LNO-380	184	91.4 ± 3.1
LNO-390	168	90.2 ± 3.4
LNO-400	158	97.6 ± 3.7
LNO-500	79	
LNO-600	58	
LNO-700	160	
LNO-850	0.2	

material. The capacity retention after 50 cycles is 64.7 ± 2.4% for LNO-200, 63.0 ± 2.1% for LNO-300, and 60.8 ± 1.8% for pristine LNO. The initial discharge capacities of these three cathodes are also close (229 mAh g^{-1} for LNO-200 and LNO, 224 mAh g^{-1} for LNO-300). When the heat treatment temperature is increased to 400 °C, the strong cation off-stoichiometric $Li_{1-z}Ni_{1+z}O_2$ and cubic phases stabilize the electrode−electrolyte interface,[34] enhancing the cycling stability obviously (capacity retention of 90.8 ± 3.5% after 200 cycles). Since there is an obvious specific capacity difference between the samples heated to 300 and 400, five more heat treatment temperatures (from 350 to 390 °C) were added in this region to investigate this in detail to further optimize the performance (Figure 9c). The specific capacities gradually decrease from 211 (LNO-350) to 168 mAh g^{-1} (LNO-390) owing to the less inactive nature of the $Li_{1-z}Ni_{1+z}O_2$ phase, but the corresponding retentions are improved step by step from 73.6 ± 2.2, 80.3 ± 2.6, 82.9 ± 3.5, 91.4 ± 3.1 to 90.2 ± 3.4% after 50 cycles. The improved cycling stability is maintained during the prolonged cycling of LNO-380 and LNO-390 cathodes. As shown in Figure 9d, the half-cells exhibit a capacity retention of 84.56% for LNO-380 and 83.44% for LNO-390 after 120 cycles. A comparison with other $LiNiO_2$ cathodes reported in previous publications is shown in Table S2. Better cycling stability can be realized when the upper voltage limit was reduced from 4.5 to 4.3 V since side reactions between the electrode and the electrolyte are stronger at high charging voltages (more unstable Ni^{4+} ions are formed and react with the electrolyte). Examples for LNO-360 and LNO-370 are displayed in Figure S26. Both samples show a formation behavior in the first few cycles, i.e., an increasing capacity. This cycling feature may be ascribed to the delayed activation of the layered LNO, in which the lithiation/delithiation processes and infiltration of electrolytes in the initial cycles were hindered by the rock-salt cubic phase at the surface.[34,35] This increase is also related to the formation of the cathode electrolyte interphase (CEI), which is more unstable under high voltages.[36] In summary, the electrochemical performance is quite sensitive to the heat treatment temper-

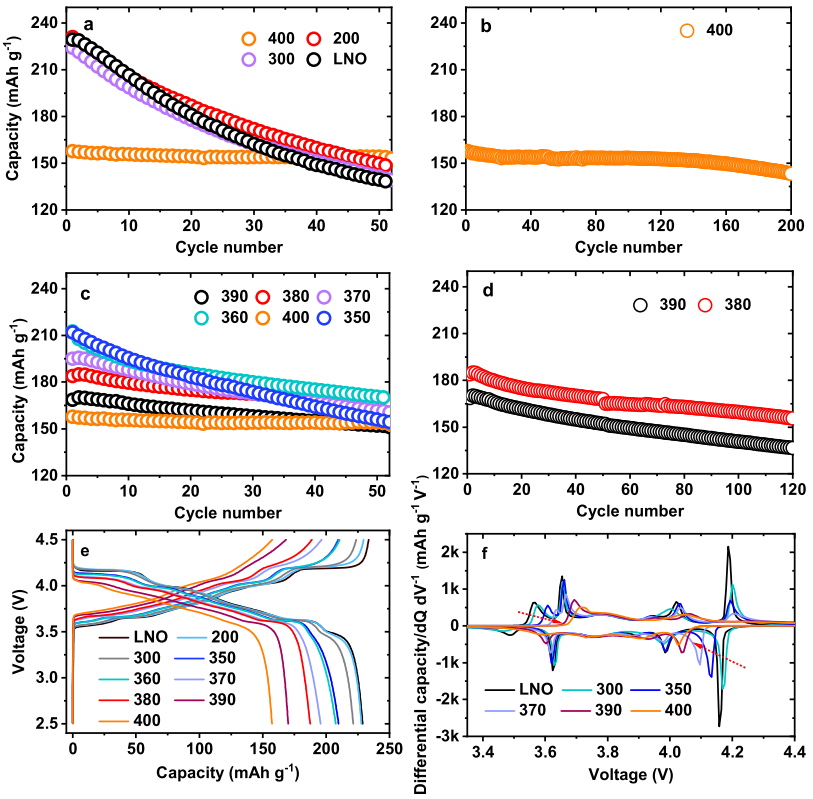

Figure 9. Electrochemical performance during galvanostatic cycling at 0.5C in the voltage range of 2.5−4.5 V: (a) pristine LNO, LNO-200, LNO-300, and LNO-400, (b) long-term cycling performance of LNO-400, (c) comparison between LNO-350, LNO-360, LNO-370, LNO-380, and LNO-390, and (d) long-term cycling performance of LNO-380 and LNO-390. (e) Cell voltages as a function of specific capacities during the first cycle of all cathodes and (f) differential capacity as a function of cell voltage (dQ/dV *vs* V) of selected cathodes. The red dashed arrows show the changes with increasing heating temperatures.

https://doi.org/10.1021/acs.chemmater.2c00995
Chem. Mater. 2022, 34, 8163−8177

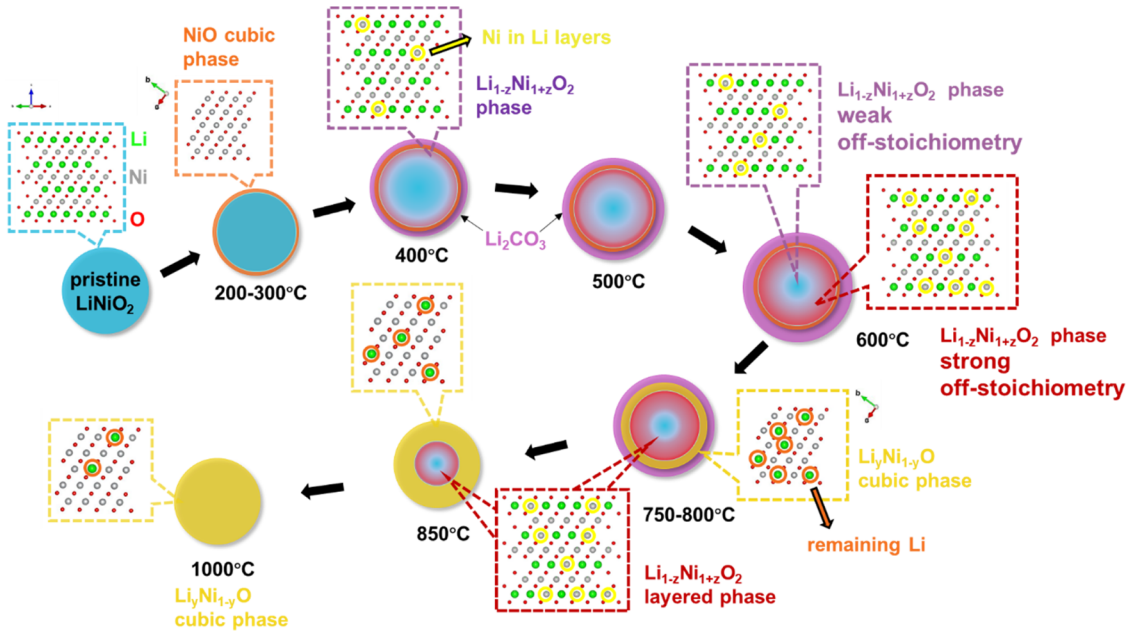

Figure 10. Scheme summarizing the process of structural changes during the heat treatment. Green spheres represent lithium, gray ones represent nickel, and red ones represent oxygen. The phase compositions of each material are displayed, including Li_2CO_3 (light purple), NiO (orange), $Li_{1-z}Ni_{1+z}O_2$ (blue for normal phase, purple for weak off-stoichiometry, and red for strong off-stoichiometry), and $Li_yNi_{1-y}O$ cubic phase (yellow).

atures between 350 and 390 °C. To better understand the effect of heat treatment on the electrochemical properties, first-cycle voltage and $dQ\ dV^{-1}$ profiles are plotted in Figure 9e,f, respectively. With increasing heat treatment temperatures, the average voltage of the voltage plateaus observed during charging is also increased. This increase is related to a larger overpotential, i.e., stronger polarization.

The observed voltage is the sum of the thermodynamic voltage of an electrochemical reaction and the overpotentials (cell impedance).[37] High-temperature treatments induce a thicker cubic phase or $Li_{1-z}Ni_{1+z}O_2$ region at the surface (see discussions in the XRD, Magnetic Measurements, and TEM sections) and therefore larger cell impedance. In the corresponding $dQ\ dV^{-1}$ curves of cathodes treated at higher temperatures, peaks that represent two-phase regions also appear at higher potentials during charging. Moreover, with increasing heat treatment temperature, an increasing peak width is observed in the voltage range of 4.15−4.27 V. This peak corresponds to the phase transition from the second hexagonal phase (H2) to the third hexagonal phase (H3).[38] The cation off-stoichiometry ($Li_{1-z}Ni_{1+z}O_2$) has been shown to disrupt Li ordering, thus establishing the behavior of solid solution and eliminating phase transitions.[39] The H2-to-H3 phase transition is crucial to the performance since it always entails large volume changes and the coexistence of two phases induces interfacial strain.[40] The release of the strain further induces cracking in electrode particles. Therefore, the suppression of the phase transition plays a key factor in improving the stability of cathodes. To confirm if this surface structure transformation is reversible, the LNO-400 cathode was reheated in pure oxygen again and tested. The same voltage profile as for the pristine LNO sample could be observed (Figure S27), which shows that the $Li_{1-z}Ni_{1+z}O_2$ or cubic surface phases could be reversibly transformed to a layered phase again. During resynthesis, Li from surface Li_2CO_3 will be incorporated into the surface lattice and local "LNO synthesis" occurs again. The electrochemical performance of samples LNO-500 and LNO-600 was also tested (Figure S28). The specific capacities are very small (below 80 mAh/g) with strong polarization effects. Interestingly, the specific capacity increases to 160 mAh g^{-1} for the LNO-700 sample (Figure S29). The abnormal increase could be ascribed to the different reaction situation during the postsynthesis thermal treatment at 700 °C: the mild bulk decomposition only induces weak cation off-stoichiometry phases throughout the material rather than strong ones mainly at the surface. The surface hindering effect is then weakened. The LNO-850 sample has almost no capacity (Figure S30), although a decreased charging/discharging rate could improve this situation. It proves the inactive electrochemical nature of the cubic $Li_{1-y}Ni_yO$ phase.

CONCLUSIONS

Pristine $LiNiO_2$ experiences several reaction regions under the postsynthesis thermal treatment in air at various temperatures. First, in region I from the pristine state to 300 °C, LNO reacts with CO_2 at an extremely low rate, forming a weakly cation off-stoichiometric $Li_{1-z}Ni_{1+z}O_2$ phase. In the second region (400−750 °C), the progress of the reaction gradually increases, and also the z value in $Li_{1-z}Ni_{1+z}O_2$ increases until 600 °C. As one product, more and more Li_2CO_3 is observed by XRD. At 700 °C, LNO decomposition occurs at a sluggish rate, and the reaction between LNO and CO_2 is suppressed. The decomposition corresponds to the increasing rate of Ni reduction, and a larger content of reduced Ni^{2+} stays in the Ni layers rather than occupying the Li vacancies. At 750 °C, cubic $Li_{1-y}Ni_yO$ is first detected by XRD. In the third region (800−1000 °C), the cubic phase quickly dominates the material and the phase transition is accompanied by huge oxygen and lithium loss. The extent of both reactions may not be homogeneous through the material, and a larger progress is found in the surface region. An ultrathin layer of ferromagnetic cubic phase therefore appears below 750 °C, verified by magnetic and TEM measurements. When the cation off-

https://doi.org/10.1021/acs.chemmater.2c00995
Chem. Mater. 2022, 34, 8163−8177

stoichiometry of $Li_{1-z}Ni_{1+z}O_2$ is not strong (namely, for heat treatments between 200 and 400 °C), the electrochemical performance of LNO could be improved with respect to the cycling stability. Our findings on the structural changes are schematically summarized in Figure 10. We believe that the postsynthesis thermal treatment could be an easy method to obtain better performance of $LiNiO_2$ and also for other Ni-based cathodes.

■ ASSOCIATED CONTENT

Supporting Information

The Supporting Information is available free of charge at https://pubs.acs.org/doi/10.1021/acs.chemmater.2c00995.

Repeated TGA measurement; galvanostatic cycling of supplementary temperature-treated LNO samples; details on Rietveld refinements and XRD Rietveld refinement patterns; details on *in situ* high-temperature SRD measurements; ^{7}Li NMR spectra of all temperature-treated LNO samples and with extended ranges; whole magnetic experiments; and supplementary STEM images and energy loss spectroscopy (PDF)

■ AUTHOR INFORMATION

Corresponding Author

Sylvio Indris − *Institute for Applied Materials (IAM), Karlsruhe Institute of Technology (KIT), 76344 Eggenstein-Leopoldshafen, Germany;* orcid.org/0000-0002-5100-113X; Email: sylvio.indris@kit.edu

Authors

Hang Li − *Institute for Applied Materials (IAM), Karlsruhe Institute of Technology (KIT), 76344 Eggenstein-Leopoldshafen, Germany*

Weibo Hua − *School of Chemical Engineering and Technology, Xi'an Jiaotong University, Xi'an, Shaanxi 710049, China;* orcid.org/0000-0001-5372-4422

Björn Schwarz − *Institute for Applied Materials (IAM), Karlsruhe Institute of Technology (KIT), 76344 Eggenstein-Leopoldshafen, Germany*

Martin Etter − *Deutsches Elektronen-Synchrotron (DESY), 22607 Hamburg, Germany*

Stefan Mangold − *Institute for Photon Science and Synchrotron Radiation, Karlsruhe Institute of Technology (KIT), 76344 Eggenstein-Leopoldshafen, Germany*

Georgian Melinte − *Institute of Nanotechnology (INT), Karlsruhe Institute of Technology (KIT), 76344 Eggenstein-Leopoldshafen, Germany*

Nicola Pietro Maria Casati − *Paul Scherrer Institute, 5232 Villigen, Switzerland;* orcid.org/0000-0002-4206-9239

Helmut Ehrenberg − *Institute for Applied Materials (IAM), Karlsruhe Institute of Technology (KIT), 76344 Eggenstein-Leopoldshafen, Germany;* orcid.org/0000-0002-5134-7130

Complete contact information is available at: https://pubs.acs.org/10.1021/acs.chemmater.2c00995

Author Contributions

H.L. and W.H. conceived the idea and conducted a discussion with S.I. and H.E. H.L carried out the preparation experiments. H.L. and S.I. performed all of the NMR measurements. B.S. conducted the magnetization measurements. H.L., W.H., and M.E. performed the synchrotron-based X-ray diffraction measurements. H.L., W.H., S.I., and N.P.M.C. conducted the *in situ* high-temperature SRD measurement. S.M. performed the XAS experiment. The data were analyzed by H.L., B.S., S.M., W.H., and S.I.. H.L. wrote the preliminary draft with input from B.S. and S.I. All authors contributed to interpreting the findings, reviewing, and revising the manuscript.

Notes

The authors declare no competing financial interest.

■ ACKNOWLEDGMENTS

H.L. received financial support from the China Scholarship Council (CSC). The authors gratefully acknowledge Valeriu Mereacre for helping with the material preparation, Liuda Mereacre for support in the lab, and Christina Odemer for the thermogravimetric analysis (TGA) measurement. The *in situ* high-temperature SRD (HTSRD) was performed at MS beamline Paul Scherer Institute (PSI) with the collaboration of PSI staff. The authors acknowledge DESY (Hamburg, Germany), a member of the Helmholtz Association HGF, for the provision of experimental facilities. Parts of this research were carried out at PETRA III at beamline P02.1. Beamtime was allocated for the proposal (Proposal ID: 20200642). The authors thank the XAS beamline of the KIT Light Source (Karlsruhe) for the X-ray absorption spectroscopy (XAS) experiment. They also thank the Karlsruhe Nano Micro Facility (KNMF, www.knmf.kit.edu), a Helmholtz Research Infrastructure at the Karlsruhe Institute of Technology (KIT, www.kit.edu), for the EELS measurement. This work contributes to the research performed at CELEST (Center for Electrochemical Energy Storage Ulm-Karlsruhe).

■ REFERENCES

(1) Darga, J.; Lamb, J.; Manthiram, A. Industrialization of Layered Oxide Cathodes for Lithium-Ion and Sodium-Ion Batteries: A Comparative Perspective. *Energy Technol.* **2020**, *8*, No. 2000723.

(2) Ryu, H. H.; Sun, H. H.; Myung, S. T.; Yoon, C. S.; Sun, Y. K. Reducing Cobalt from Lithium-Ion Batteries for the Electric Vehicle Era. *Energy Environ. Sci.* **2021**, *14*, 844−852.

(3) Wang, X.; Ding, Y. L.; Deng, Y. P.; Chen, Z. Ni-Rich/Co-Poor Layered Cathode for Automotive Li-Ion Batteries: Promises and Challenges. *Adv. Energy Mater.* **2020**, *10*, No. 1903864.

(4) Liu, T.; Yu, L.; Liu, J.; Lu, J.; Bi, X.; Dai, A.; Li, M.; Li, M.; Hu, Z.; Ma, L.; Luo, D.; Zheng, J.; Wu, T.; Ren, Y.; Wen, J.; Pan, F.; Amine, K. Understanding Co Roles towards Developing Co-Free Ni-Rich Cathodes for Rechargeable Batteries. *Nat. Energy* **2021**, *6*, 277−286.

(5) Dyer, L. D.; Borie, B. S.; Smith, G. P. Alkali Metal-Nickel Oxides of the Type $MNiO_2$. *J. Am. Chem. Soc.* **1954**, *76*, 1499−1503.

(6) Dahn, J. R.; von Sacken, U.; Michal, C. A. Structure and Electrochemistry of $Li_{1\pm y}NiO_2$ and a New Li_2NiO_2 Phase with the $Ni(OH)_2$ Structure. *Solid State Ionics* **1990**, *44*, 87−97.

(7) Delmas, C.; Peres, J. P.; Rougier, A.; Demourgues, A.; Weill, F.; Chadwick, A.; Broussely, M.; Perton, F.; Biensan, P.; Willmann, P. On the Behavior of the Li_xNiO_2 System: An Electrochemical and Structural Overview. *J. Power Sources* **1997**, *68*, 120−125.

(8) Delmas, C.; Ménétrier, M.; Croguennec, L.; Saadoune, I.; Rougier, A.; Pouillerie, C.; Prado, G.; Grüne, M.; Fournes, L. An Overview of the $Li(Ni,M)O_2$ Systems: Syntheses, Structures and Properties. *Electrochim. Acta* **1999**, *45*, 243−253.

(9) Bianchini, M.; Fauth, F.; Hartmann, P.; et al. An *in Situ* Structural Study on the Synthesis and Decomposition of $LiNiO_2$. *J. Mater. Chem. A* **2020**, *8*, 1808−1820.

(10) McCalla, E.; Carey, G. H.; Dahn, J. R. Lithium Loss Mechanisms during Synthesis of Layered $Li_xNi_{2-x}O_2$ for Lithium Ion Batteries. *Solid State Ionics* **2012**, *219*, 11−19.

(11) Zhang, M. J.; Hu, X.; Li, M.; Duan, Y.; Yang, L.; Yin, C.; Ge, M.; Xiao, X.; Lee, W. K.; Ko, J. Y. P.; Amine, K.; Chen, Z.; Zhu, Y.; Dooryhee, E.; Bai, J.; Pan, F.; Wang, F. Cooling Induced Surface Reconstruction during Synthesis of High-Ni Layered Oxides. *Adv. Energy Mater.* **2019**, *9*, No. 1901915.
(12) Haik, O.; Leifer, N.; Samuk-Fromovich, Z.; Zinigrad, E.; Markovsky, B.; Larush, L.; Goffer, Y.; Goobes, G.; Aurbach, D. On the Surface Chemistry of $LiMO_2$ Cathode Materials (M = [MnNi] and [MnNiCo]): Electrochemical, Spectroscopic, and Calorimetric Studies. *J. Electrochem. Soc.* **2010**, *157*, A1099.
(13) Eom, J.; Kim, M. G.; Cho, J. Storage Characteristics of $LiNi_{0.8}Co_{0.1+x}Mn_{0.1-x}O_2$ (x = 0, 0.03, and 0.06) Cathode Materials for Lithium Batteries. *J. Electrochem. Soc.* **2008**, *155*, A239.
(14) Guilmard, M.; Croguennec, L.; Denux, D.; Delmas, C. Thermal Stability of Lithium Nickel Oxide Derivatives. Part I: $Li_xNi_{1.02}O_2$ and $Li_xNi_{0.89}Al_{0.16}O_2$ (x = 0.50 and 0.30). *Chem. Mater.* **2003**, *15*, 4476−4483.
(15) Nam, K. W.; Bak, S. M.; Hu, E.; Yu, X.; Zhou, Y.; Wang, X.; Wu, L.; Zhu, Y.; Chung, K. Y.; Yang, X. Q. Combining in Situ Synchrotron X-Ray Diffraction and Absorption Techniques with Transmission Electron Microscopy to Study the Origin of Thermal Instability in Overcharged Cathode Materials for Lithium-Ion Batteries. *Adv. Funct. Mater.* **2013**, *23*, 1047−1063.
(16) Marks, T.; Trussler, S.; Smith, A. J.; Xiong, D.; Dahn, J. R. A Guide to Li-Ion Coin-Cell Electrode Making for Academic Researchers. *J. Electrochem. Soc.* **2011**, *158*, A51.
(17) Willmott, P.; Meister, D.; Leake, S.; Lange, M.; Bergamaschi, A.; Böge, M.; Calviom; Cancellieri, C.; Casati, N.; Cervellino, A.; Chen, Q.; David, C.; Flechsig, U.; Gozzo, F.; Henrich, B.; Jäggi-Spielmann, S.; Jakob, B.; Kalichava, I.; Karvinen, P.; Krempasky, J.; Lüdeke, A.; Lüscher, R.; Maag, S.; Quitmann, C.; Reinle-Schmitt, M.; Schmidt, T.; Schmitt, B.; Streun, A.; Vartiainen, I.; Vitins, M.; Wang, X.; Wullschleger, R. The Materials Science Beamline Upgrade at the Swiss Light Source. *J. Synchrotron Radiat.* **2013**, *20*, 667−682.
(18) Rodríguez-Carvajal, J. Recent Advances in Magnetic Structure Determination by Neutron Powder Diffraction. *Phys. B Condens. Matter* **1993**, *192*, 55−69.
(19) Ravel, B.; Newville, M. ATHENA, ARTEMIS, HEPHAESTUS: Data Analysis for X-Ray Absorption Spectroscopy Using IFEFFIT. *J. Synchrotron Radiat.* **2005**, *12*, 537−541.
(20) Liu, H.; Yang, Y.; Zhang, J. Reaction Mechanism and Kinetics of Lithium Ion Battery Cathode Material $LiNiO_2$ with CO_2. *J. Power Sources* **2007**, *173*, 556−561.
(21) Sata, T. High-Temperature Vaporization of Li_2O Component from Solid Solution $Li_xNi_{1-x}O$ in Air. *Ceram. Int.* **1998**, *24*, 53−59.
(22) Kim, J. W.; Lee, H. G. Thermal and Carbothermic Decomposition of Na_2CO_3 and Li_2CO_3. *Metall. Mater. Trans. B* **2001**, *32*, 17−24.
(23) Grey, C. P.; Dupré, N. NMR Studies of Cathode Materials for Lithium-Ion Rechargeable Batteries. *Chem. Rev.* **2004**, *104*, 4493−4512.
(24) Märker, K.; Reeves, P. J.; Xu, C.; Griffith, K. J.; Grey, C. P. Evolution of Structure and Lithium Dynamics in $LiNi_{0.8}Mn_{0.1}Co_{0.1}O_2$ (NMC811) Cathodes during Electrochemical Cycling. *Chem. Mater.* **2019**, *31*, 2545−2554.
(25) Kim, U. H.; Jun, D. W.; Park, K. J.; Zhang, Q.; Kaghazchi, P.; Aurbach, D.; Major, D. T.; Goobes, G.; Dixit, M.; Leifer, N.; Wang, C. M.; Yan, P.; Ahn, D.; Kim, K. H.; Yoon, C. S.; Sun, Y. K. Pushing the Limit of Layered Transition Metal Oxide Cathodes for High-Energy Density Rechargeable Li Ion Batteries. *Energy Environ. Sci.* **2018**, *11*, 1271−1279.
(26) Li, H.; Hua, W.; Liu-Théato, X.; Fu, Q.; Desmau, M.; Missyul, A.; Knapp, M.; Ehrenberg, H.; Indris, S. New Insights into Lithium Hopping and Ordering in $LiNiO_2$ Cathodes during Li (De)-Intercalation. *Chem. Mater.* **2021**, *33*, 9546−9559.
(27) Grenier, A.; Reeves, P. J.; Liu, H.; Seymour, I. D.; Märker, K.; Wiaderek, K. M.; Chupas, P. J.; Grey, C. P.; Chapman, K. W. Intrinsic Kinetic Limitations in Substituted Lithium-Layered Transition-Metal Oxide Electrodes. *J. Am. Chem. Soc.* **2020**, *142*, 7001−7011.
(28) Chappel, E.; Núñez-Regueiro, M. D.; De Brion, S.; Chouteau, G.; Bianchi, V.; Caurant, D.; Baffier, N. Interlayer Magnetic Frustration in Quasistoichiometric (formula presented). *Phys. Rev. B* **2002**, *66*, No. 132412.
(29) Srinivasan, G.; Seehra, M. S. Magnetic Susceptibilities, Their Temperature Variation, and Exchange Constants of NiO. *Phys. Rev. B* **1984**, *29*, 6295−6298.
(30) Sugiyama, J.; Ikedo, Y.; Mukai, K.; Nozaki, H.; Månsson, M.; Ofer, O.; Harada, M.; Kamazawa, K.; Miyake, Y.; Brewer, J. H.; Ansaldo, E. J.; Chow, K. H.; Watanabe, I.; Ohzuku, T. Low-Temperature Magnetic Properties and High-Temperature Diffusive Behavior of $LiNiO_2$ Investigated by Muon-Spin Spectroscopy. *Phys. Rev. B* **2010**, *82*, No. 224412.
(31) Julien, C. M.; Ait-Salah, A.; Mauger, A.; Gendron, F. Magnetic Properties of Lithium Intercalation Compounds. *Ionics* **2006**, *12*, 21−32.
(32) Shimomura, Y.; Kojima, M.; Saito, S. Crystal Structure of Ferromagnetic Nickel Oxide. *J. Phys. Soc. Jpn.* **1956**, *11*, 1136−1146.
(33) Nellist, P. D.The Principles of STEM Imaging. In *Scanning Transmission Electron Microscopy*; Springer: New York, NY, 2011; pp 91−115.
(34) Jo, J. H.; Jo, C. H.; Yashiro, H.; Kim, S. J.; Myung, S. T. Re-Heating Effect of Ni-Rich Cathode Material on Structure and Electrochemical Properties. *J. Power Sources* **2016**, *313*, 1−8.
(35) Huang, G.-X.; Wang, R.-H.; Lv, X.-Y.; Su, J.; Long, Y.-F.; Qin, Z.-Z.; Wen, Y.-X. Effect of Niobium Doping on Structural Stability and Electrochemical Properties of $LiNiO_2$ Cathode for Li-Ion Batteries. *J. Electrochem. Soc.* **2022**, *169*, No. 040533.
(36) Antonopoulos, B. K.; Stock, C.; Maglia, F.; Hoster, H. E. Solid Electrolyte Interphase: Can Faster Formation at Lower Potentials Yield Better Performance? *Electrochim. Acta* **2018**, *269*, 331−339.
(37) Kurzhals, P.; Riewald, F.; Bianchini, M.; Sommer, H.; Gasteiger, H. A.; Janek, J. The $LiNiO_2$ Cathode Active Material: A Comprehensive Study of Calcination Conditions and Their Correlation with Physicochemical Properties. Part I. Structural Chemistry. *J. Electrochem. Soc.* **2021**, *168*, No. 110518.
(38) Li, W.; Reimers, J. N.; Dahn, J. R. In Situ X-Ray Diffraction and Electrochemical Studies of $Li_{1-x}NiO_2$. *Solid State Ionics* **1993**, *67*, 123−130.
(39) Mock, M.; Bianchini, M.; Fauth, F.; Albe, K.; Sicolo, S. Atomistic Understanding of the $LiNiO_2$-NiO_2 phase Diagram from Experimentally Guided Lattice Models. *J. Mater. Chem. A* **2021**, *9*, 14928−14940.
(40) Yoon, C. S.; Jun, D. W.; Myung, S. T.; Sun, Y. K. Structural Stability of $LiNiO_2$ Cycled above 4.2V. *ACS Energy Lett.* **2017**, *2*, 1150−1155.

https://doi.org/10.1021/acs.chemmater.2c00995
Chem. Mater. 2022, 34, 8163−8177